

Near-Field Source Localization and Beamforming in the Spherical Sector Harmonics Domain

Shekhar Kumar Yadav, *Graduate Student Member, IEEE*, S. R. M. Prasanna, *Senior Member, IEEE* and Nithin V. George, *Member, IEEE*

Abstract—Three-dimensional arrays have the ability to localize sources anywhere in the spatial domain without any ambiguity. Among these arrays, the spherical microphone array (SMA) has gained widespread usage in acoustic source localization and beamforming. However, SMAs are bulky and in many applications with space and power constraints, it is undesirable to use an SMA. To deal with this issue, arrays with microphones placed only in a sector of a sphere have been developed along with various techniques for localizing far-field sources in the spherical sector harmonics (S^2H) domain. This work addresses near-field acoustic localization and beamforming using a spherical sector microphone array. We first introduce a representation of spherical waves from a near-field point source in the S^2H domain using the orthonormal S^2H basis functions. Then, using the representation, we develop an array model for when a spherical sector array is placed in a wavefield created by multiple near-field sources in the S^2H domain. We highlight the advantages of the developed array model over the baseline near-field spatial domain array model. Using the developed array model, two algorithms are proposed for the joint estimation of the range, elevation and azimuth locations of near-field sources, namely NF- S^2H -MUSIC and NF- S^2H -MVDR. Further, a near-field beamforming algorithm capable of radial and angular filtering in the S^2H domain is also presented. Finally, we present the Cramer-Rao Bound (CRB) for range, elevation and azimuth estimation in the S^2H domain for near-field sources. The performances of the proposed algorithms are assessed using extensive near-field localization and beamforming simulations and an experiment.

Index Terms—Microphone array, Near-field, Spherical sector harmonics, Source localization, MUSIC, Beamforming, MVDR

I. INTRODUCTION

SOURCE localization refers to the process of determining the spatial location of a particular signal or source of interest within a given environment. It involves identifying the location from which a particular signal, sound, electromagnetic wave, or other phenomenon originates, and it is widely used in fields like acoustics, wireless communication, geophysics, medical diagnostics, and robotics to gain insights into the source's location or to track and analyze its movements. Usually, an array of sensors placed in a particular geometry is

used for source localization. For sources in the far-field of the array, source localization refers to estimating the direction of arrival (DOA) of the source whereas for near-field sources, it refers to estimating the range, elevation and azimuth location of the source. Many source localization techniques exist in the literature that use linear and planar arrays for far-field and near-field localization [1]. The most common among them are the subspace-based techniques of Multiple signal classification (MUSIC) [2] and Estimation of signal parameters via rotational invariance technique (ESPRIT) [3]. However, linear and planar arrays have spatial ambiguities, which prevent them from covering the entire three-dimensional (3D) space [4].

To remove spatial ambiguities, 3D arrays are used. Spherical arrays are a class of 3D arrays that can cover the entire 3D space not only without any ambiguities but also with equal resolution in all directions [5]. Spherical arrays also facilitate processing within the spherical harmonics (SH) domain, providing numerous benefits for array processing, such as separability of frequency and angular components of signals. Many source localization and beamforming techniques have been developed in the SH domain, especially for acoustic signals using spherical microphone arrays [6]–[13]. MUSIC and ESPRIT algorithms were developed in the SH domain in [14]–[16]. A deep-learning framework was developed in [17] for robust estimation of DOAs using SH decomposition. Bayesian learning based approaches for source localization using spherical arrays were developed in [18], [19]. In [7], the minimum variance distortionless response (MVDR) beamforming method [20] was introduced in the SH domain for DOA estimation. Most of the work in the SH domain discussed thus far deals with planar wavefronts of far-field sources. But in applications where the source is in the near-field of the array such as video conferencing, human-robot interaction, music recording, etc., the planar wavefront is invalid and may lead to errors. The near-field sources emit spherical waves, which must be considered in the array signal model [21]. In [22], [23], near-field techniques capable of radial filtering were developed in the SH domain. Various acoustic source localization techniques for near-field sources based on the principles of MUSIC and MVDR were presented in [24], [25] in the SH domain. A time domain near-field beamformer that utilized spherical harmonics decomposition was recently proposed in [26].

In many applications, processing signals from all the microphones of a spherical array may be computationally burdensome. Also, using an entire spherical array may not be feasible in applications with space constraints. Array processing

This work is supported by the TEOCO Chair of the Indian Institute of Technology Gandhinagar. S. K. Yadav was with the Department of Electrical Engineering, Indian Institute of Technology Gandhinagar, India, till July 2024 (e-mail: yadav_shekhar@iitgn.ac.in). S.R.M. Prasanna is the Director of the Indian Institute of Information Technology Dharwad (IIIT Dharwad) and a Professor in the Department of Data Science and Artificial Intelligence, IIIT Dharwad. He is also associated with the Department of Electrical, Electronics and Communication Engineering at the Indian Institute of Technology Dharwad (email: prasanna@iiitdwd.ac.in). N. V. George is an Associate Professor in the Department of Electrical Engineering, Indian Institute of Technology Gandhinagar, India (e-mail: nithin@iitgn.ac.in).

techniques for hemispherical arrays mounted on the ceiling or the top of a conference table have been developed [27]–[29]. Recently, microphone arrays where the microphones are placed only in an arbitrary sector of a sphere have also been developed [30]. The orthonormal basis function of the spherical sector harmonics (S²H) was introduced in [31], which is a generalized version of the SH basis function. The S²H basis function becomes the SH basis function when the sector is the entire sphere. Far-field acoustic localization and beamforming methods using spherical sector microphone array (S²MA) were proposed in [30] in the S²H domain. Optimal beamformer designs and S²H norm applied to blind source separation were presented in [32], [33]. An S²H domain based noise reduction technique to reduce directional drone tonal noise was developed in [34], and an S²H domain based soundfield radial extrapolation method was proposed in [35].

In this work, we propose techniques for acoustic localization and beamforming for near-field sources using an S²MA. We first introduce a representation of spherical waves from a near-field point source in the S²H domain using the S²H basis function, based on which a novel array data model is developed for near-field sources. We discuss the advantages of the proposed array model over the baseline spatial domain near-field array model. Using the developed model, we propose techniques to simultaneously estimate the range, elevation and azimuth location of the near-field sources in the S²H domain. Additionally, our work presents beamforming and Cramer-Rao bound (CRB) analysis for near-field sources in the S²H domain. We also present a computational complexity analysis of the proposed algorithms. Extensive simulations and a practical experiment have been presented to demonstrate the effectiveness of the proposed algorithms.

Notations: Bold case upper and lower case letters represent matrices and vectors, respectively. $(\cdot)^T$, $(\cdot)^*$ and $(\cdot)^H$ denotes the transpose, conjugate and conjugate transpose operations, respectively. \mathbb{E} represents the mathematical expectation operator and $\|\cdot\|$ represents the ℓ_2 -norm of a vector. $|\cdot|$, $\text{Re}\{\cdot\}$ and $\text{Im}\{\cdot\}$ denote a complex number's magnitude, real and imaginary part, respectively. \odot represents the Hadamard product.

II. SPHERICAL WAVE SPREADING FROM A POINT SOURCE

We consider a microphone array where Q microphones are placed on a sector of a sphere whose centre is at the origin, as shown in Fig. 1. The sector is defined in terms of elevation range $[\theta_1, \theta_2]$, azimuth range $[\phi_1, \phi_2]$ and the radius r_a of the spherical sector. The elevation angle is calculated down from the positive z-axis and the azimuth angle is calculated anti-clockwise from the positive x-axis. The location of the q^{th} microphone is denoted as $\mathbf{r}_q = (r_a, \Phi_q)$ where $\Phi_q = (\theta_q, \phi_q)$. Now, we assume that a near-field point source emitting unit-amplitude spherical waves with wavenumber k is present at location $\mathbf{r}_l = (r_l, \Psi_l)$ where $\Psi_l = (\theta_l, \phi_l)$. In a homogeneous fluid with no viscosity, the incident sound pressure P_{in} of the spherical wave at an observation point \mathbf{r}_q satisfies the following inhomogeneous Helmholtz equation in the frequency domain [36]–[38]

$$\nabla^2 P_{in}(\mathbf{r}_q, \mathbf{r}_l, \omega) + k^2 P_{in}(\mathbf{r}_q, \mathbf{r}_l, \omega) = -\delta(\mathbf{r}_q - \mathbf{r}_l), \quad (1)$$

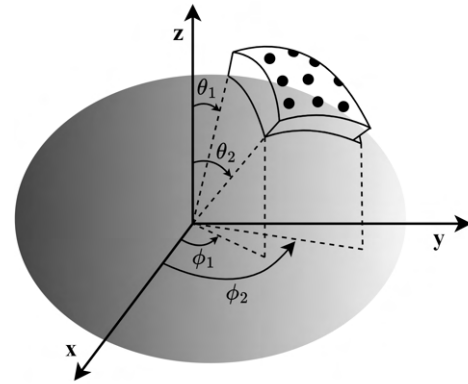


Fig. 1. A microphone array on a sector of a sphere of radius r_a . The sector is defined by the angular region of elevation $[\theta_1, \theta_2]$ and azimuth $[\phi_1, \phi_2]$.

where $\omega = 2\pi f$ (f is the frequency) is related to the wavenumber as $k = \omega/c$ (c is the speed of the sound wave). δ is the Kronecker delta function. ∇^2 is the Laplacian operator, which is expressed in the spherical coordinates as

$$\nabla^2 = \frac{1}{r_q^2} \frac{\partial}{\partial r_q} \left(r_q^2 \frac{\partial}{\partial r_q} \right) + \frac{1}{r_q^2 \sin \theta_q} \frac{\partial}{\partial \theta_q} \left(\sin \theta_q \frac{\partial}{\partial \theta_q} \right) + \frac{1}{\sin^2 \theta_q} \frac{\partial^2}{\partial \phi_q^2}. \quad (2)$$

Since a microphone at the observation point absorbs the sound wave, the solution to (1) in the spatial domain is given as [38]

$$P_{in}(\mathbf{r}_q, \mathbf{r}_l, \omega) = \frac{e^{-ik\|\mathbf{r}_q - \mathbf{r}_l\|}}{4\pi\|\mathbf{r}_q - \mathbf{r}_l\|}. \quad (3)$$

The solution assumes that no scattering occurs at the observation point, i.e. the microphone is placed on an open spherical sector. Our aim is to represent the pressure in (3) in the S²H domain. So, in the next subsection, we introduce S²H decomposition and its basis function.

A. S²H Decomposition

A function over any arbitrary spherical sector, in our case $P_{in}(\mathbf{r}_q, \mathbf{r}_l, \omega)$, can be transformed into the S²H domain by using the following transformation [31]

$$P_{nm}(\mathbf{r}_l, r_a, \omega) = \int_{\Phi \in S^2} P_{in}(\mathbf{r}_q, \mathbf{r}_l, \omega) [T_n^m(\Phi)]^* d\Phi, \quad (4)$$

where $\int_{\Phi \in S^2}$ represents the solid angle $\int_{\phi_1}^{\phi_2} \int_{\theta_1}^{\theta_2} \sin \theta d\theta d\phi$ of a unit radius spherical sector. $P_{nm}(\mathbf{r}_l, r_a, \omega)$ are referred to as the coefficients of $P_{in}(\mathbf{r}_q, \mathbf{r}_l, \omega)$ in the S²H domain. $T_n^m(\Phi)$ is the basis function of the S²H domain of order n and degree m and is expressed as

$$T_n^m(\Phi) = \begin{cases} C_n^m \tilde{\mathcal{P}}_n^m(\cos \theta) \tilde{e}^{im\phi}, & \forall 0 \leq n < \infty, 0 \leq m \leq n \\ (-1)^{|m|} |T_n^m|^*(\Phi), & \forall -n \leq m < 0. \end{cases} \quad (5)$$

We now define each term in (5) and establish that $T_n^m(\Phi)$ is orthonormal. $\tilde{\mathcal{P}}_n^m(x)$ is the shifted associated Legendre polynomial (ALP) of order n and degree m obtained by

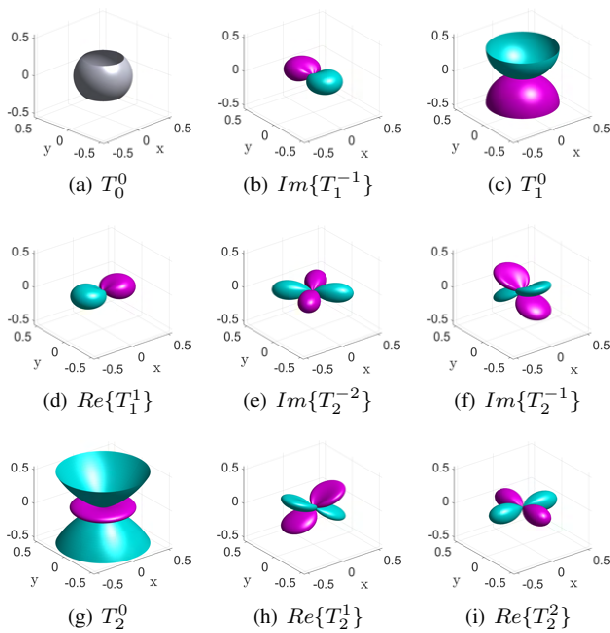


Fig. 2. Spherical sector harmonics (T_n^m) for a sector defined by $\theta \in [45^\circ, 135^\circ]$ and $\phi \in [0^\circ, 360^\circ]$ ($\alpha_1 = 1.4142$, $\alpha_2 = 0$ and $\beta = 1$) of unit radius. The order is varied from $n = 0, 1, 2$.

shifting the ALP $\mathcal{P}_n^m(x)$. Over the range $x \in [-1, 1]$, the ALP is orthogonal with weighting function $w(x) = 1$ according to the following relation [5]

$$\int_{-1}^1 w(x) \mathcal{P}_n^m(x) \mathcal{P}_n^m(x) dx = \frac{2(n+m)!}{(2n+1)(n-m)!} \delta_{nn}. \quad (6)$$

Putting $x = \cos \theta$, the ALP $\mathcal{P}_n^m(\cos \theta)$ is orthogonal over the elevation range of $\theta \in [0, \pi]$. For the elevation range of $\theta \in [\theta_1, \theta_2]$ for a spherical sector, an orthogonality relation is established by shifting the ALP [31]. The shift is achieved by a linear transformation on x and the shifted ALP $\tilde{\mathcal{P}}_n^m(x)$ is given as

$$\tilde{\mathcal{P}}_n^m(x) = \mathcal{P}_n^m(\alpha_1 x + \alpha_2), \quad (7)$$

where $\alpha_1 \neq 0$. If $\mathcal{P}_n^m(x)$ is orthogonal over the range $[a, b]$ with weighting factor $w(x)$, then the shifted ALP $\tilde{\mathcal{P}}_n^m(x)$ is orthogonal over the range $[\frac{a-\alpha_2}{\alpha_1}, \frac{b-\alpha_2}{\alpha_1}]$ with weighting factor $w(\alpha_1 x + \alpha_2)$ [31]. The orthogonality relation with $w(\alpha_1 x + \alpha_2) = 1$ is given by

$$\int_{(a-\alpha_2)/\alpha_1}^{(b-\alpha_2)/\alpha_1} \tilde{\mathcal{P}}_n^m(x) \tilde{\mathcal{P}}_n^m(x) dx = \frac{1}{\alpha_1} \frac{2(n+m)!}{(2n+1)(n-m)!} \delta_{nn}. \quad (8)$$

To define $\tilde{e}^{im\phi}$ in (5), we first note that the function $e^{im\phi}$ is orthogonal over the entire spherical azimuth range of $\phi \in [0, 2\pi]$ and the orthogonal relation is given by

$$\int_0^{2\pi} e^{im\phi} e^{-im\phi} d\phi = 2\pi \delta_{mm}. \quad (9)$$

For a spherical sector, the azimuth range can be specified by $\phi \in [0, 2\pi/\beta]$ where $\beta \geq 1$. To achieve orthogonality in this range, the scaled exponential function $\tilde{e}^{im\phi}$ is defined by

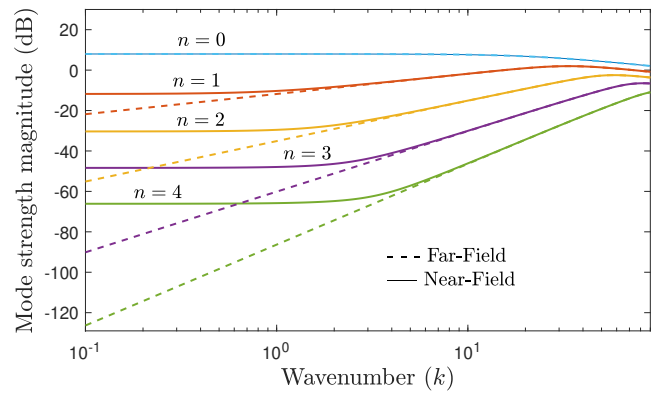


Fig. 3. The magnitude of far-field and near-field mode strength for a rigid spherical sector array for different array order. The sector considered is a hemisphere ($\alpha_1 = 2$, $\alpha_2 = -1$ and $\beta = 1$) of radius 4.2cm . The near-field source is placed at a distance of $r = 1\text{m}$ from the array. We can see that for lower kr , the near-field mode strength dominates, while for higher kr , near-field mode strength becomes the far-field mode strength.

replacing ϕ in $e^{im\phi}$ with $\beta\phi$. The orthogonality relation of the scaled exponential function is given by

$$\int_{\phi_1}^{\phi_2} \tilde{e}^{im\phi} \tilde{e}^{-im\phi} d\phi = \frac{2\pi}{\beta} \delta_{mm}, \quad (10)$$

where $\phi_1 = 0$ and $\phi_2 = 2\pi/\beta$. Combining the elevation and the azimuth orthogonal function for a spherical sector in (8) and (10), respectively, we get the orthonormality relation of the S^2H domain basis function as

$$\int_{\phi_1}^{\phi_2} \int_{\theta_1}^{\theta_2} T_n^m(\theta, \phi) [T_n^m(\theta, \phi)]^* \sin \theta d\theta d\phi = \delta_{nn} \delta_{mm}. \quad (11)$$

The normalization constant C_n^m in (5), given by

$$C_n^m = \sqrt{\frac{(2n+1)(n-m)! (\alpha_1 \beta)}{4\pi(n+m)!}}, \quad (12)$$

is defined such that $T_n^m(\theta, \phi)$ is orthonormal and not just orthogonal. Real and imaginary parts of some S^2H domain basis functions for a sector defined by $\theta \in [45^\circ, 135^\circ]$ and $\phi \in [0^\circ, 360^\circ]$ of unit radius are plotted in Fig. 2. The description of S^2H transformation of a function defined over a spherical sector is now complete. The inverse S^2H transform of (4) to get the pressure from the coefficients is expressed as

$$P_{in}(\mathbf{r}_q, \mathbf{r}_l, \omega) = \sum_{n=0}^{\infty} \sum_{m=-n}^n P_{nm}(\mathbf{r}_l, r_a, \omega) T_n^m(\Phi). \quad (13)$$

B. Spherical Wave in S^2H domain

In this subsection, we introduce the representation of the spherical wave solution in (3) in the S^2H domain. Using the S^2H transformation, the sound pressure from a spherical wave in (3) can be written as

$$\frac{e^{-ik\|\mathbf{r}_q - \mathbf{r}_l\|}}{\|\mathbf{r}_q - \mathbf{r}_l\|} = \sum_{n=0}^{\infty} \sum_{m=-n}^n \tilde{b}_n(k, r_l, r_a) [T_n^m(\Psi_l)]^* T_n^m(\Phi_q), \quad (14)$$

where $\tilde{b}_n(k, r_l, r_a)$ is defined as the strength of the n^{th} order near-field mode in the S²H domain. It relates to the n^{th} order strength of the S²H domain far-field mode $\tilde{b}_n(k, r_a)$ as [22], [24]

$$\tilde{b}_n(k, r_l, r_a) = i^{-(n-1)} k \tilde{b}_n(k, r_a) h_n(kr_l), \quad (15)$$

where h_n is the spherical Hankel function of the second kind. The far-field mode strength in the S²H domain is given by [31]

$$\tilde{b}_n(k, r) = \begin{cases} \frac{4\pi i^n}{\alpha_1^{(n+1)\beta}} j_n(kr) & : \text{open sector} \\ \frac{4\pi i^n}{\alpha_1^{(n+1)\beta}} \left(j_n(kr) - \frac{j'_n(kr_a)}{h'_n(kr_a)} h_n(kr) \right) & : \text{rigid sector}, \end{cases} \quad (16)$$

where j_n is the spherical Bessel function of the first kind and $(\cdot)'$ denotes the first derivative. The second term in the far-field mode strength for a rigid spherical sector is due to the scattering that occurs on the surface of the rigid sector of radius r_a . Also, from (15), we see that the Hankel function captures the range of the near-field source. This shines a light on how the radial information of the source is captured in the S²H domain, which is not immediately discernible in the spatial domain. Note that $j_n(kr_a)$ becomes negligible as $n \gg kr_a$ [7], so for higher order n , the strength of the far-field mode and, by extension, the strength of the near-field mode diminishes. Thus, we can truncate the summation in (14) to a sufficiently high finite order N without introducing significant errors.

We now present a condition that the radial distance of the source has to satisfy for it to be considered a near-field source in the S²H domain. The condition is based on the mode strength rather than the Fraunhofer distance [21]. From the S²H near-field and far-field mode strength expressions, the two become similar when $kr_l \approx N$ as shown in Fig. 3. So, the near-field radial boundary should be

$$r_{nf} \approx \frac{N}{k}. \quad (17)$$

Also, the near-field source has to be outside the spherical sector, so $r_l \geq r_a$. So, the radial distance for a near-field source should satisfy

$$r_a \leq r_l \leq r_a \frac{k_{\max}}{k}, \quad (18)$$

where $k_{\max} = N/r_a$. Thus, a spherical sector array's near-field is defined by the frequency of operation and the highest order of the spherical sector harmonics. Also, lower frequencies have a larger near-field extent than higher frequencies. Moreover, the near-field extent of a spherical sector array can be increased by sampling the array beyond just satisfying the spatial aliasing condition ($k_{\max} > N/r_a$). Beyond the range in (18), the source can be considered to be in the far field of the array in the S²H domain.

III. PROPOSED NEAR-FIELD SPHERICAL SECTOR ARRAY DATA MODEL IN S²H DOMAIN

With all the information presented in the previous section, we now develop the array model of a spherical sector array with

Q microphones placed in the wavefield of L near-field sources emitting spherical waves in the S²H domain. Once again, the location of the q^{th} microphone and the l^{th} source are denoted as \mathbf{r}_q and \mathbf{r}_l , respectively. In a non-reverberant environment, at discrete time instant t , the pressure at the q^{th} microphone due to the signal $s_l(t)$ from the l^{th} near-field source is given by

$$p_{ql}(t) = \frac{s_l(t - \tau_q(\Psi_l))}{\|\mathbf{r}_q - \mathbf{r}_l\|}, \quad (19)$$

where $\tau_q(\Psi_l)$ is the time-delay of the signal between the two points \mathbf{r}_q and \mathbf{r}_l and is expressed as $\tau_q(\Psi_l) = \frac{\|\mathbf{r}_q - \mathbf{r}_l\|}{c}$. The total pressure at the q^{th} microphone from all the L sources is

$$p_q(t) = \sum_{l=1}^L \frac{s_l(t - \tau_q(\Psi_l))}{\|\mathbf{r}_q - \mathbf{r}_l\|} + g_q(t), \quad (20)$$

where $g_q(t)$ is the additive noise at the q^{th} microphone. The noise is assumed to be uncorrelated to the source signals. The total number of time snapshots considered is N_s , i.e. $t = 1, 2, \dots, N_s$. Applying discrete Fourier transform (DFT) to (20), we get

$$P_q(f_\nu) = \sum_{l=1}^L \frac{e^{-i2\pi f_\nu \tau_q(\Psi_l)}}{\|\mathbf{r}_q - \mathbf{r}_l\|} S_l(f_\nu) + G_q(f_\nu), \quad (21)$$

$\nu = 1, 2, \dots, N_s,$

where the frequency f_ν is related to the FFT index \mathcal{I}_ν as $f_\nu = \frac{\mathcal{I}_\nu}{T_s N_s}$ (T_s is the sampling frequency). $S_l(f_\nu)$ and $G_q(f_\nu)$ are the FFT of $s_l(t)$ and $g_q(t)$, respectively. Putting the expression of $\tau_q(\Psi_l)$ in (21) with $k_\nu = 2\pi f_\nu / c$, we get the total pressure at the q^{th} microphone in the frequency domain as

$$P_q(k) = \sum_{l=1}^L \frac{e^{-ik\|\mathbf{r}_q - \mathbf{r}_l\|}}{\|\mathbf{r}_q - \mathbf{r}_l\|} S_l(k) + G_q(k). \quad (22)$$

We have dropped ν from (22) for notational simplicity. Combining the pressure at all the Q microphones into a matrix form, we finally get the near-field spherical sector signal model as

$$\mathbf{P}(k) = \mathbf{V}(r, \Psi) \mathbf{S}(k) + \mathbf{G}(k) \quad (23)$$

where $\mathbf{P}(k) = [P_1(k), P_2(k), \dots, P_Q(k)]^T$, $\mathbf{S}(k)$ is the $L \times N_s$ signal matrix and $\mathbf{G}(k)$ is the $Q \times N_s$ noise matrix. $\mathbf{V}(r, \Psi)$ is the $Q \times L$ steering matrix that contains the delay information of all the near-field sources to all the microphones and is expressed as

$$\mathbf{V}(r, \Psi) = [\mathbf{v}(r_1, \Psi_1), \mathbf{v}(r_2, \Psi_2), \dots, \mathbf{v}(r_L, \Psi_L)], \quad (24)$$

where $\mathbf{v}(r_l, \Psi_l)$ is the steering vector of the l^{th} source given by (dependence of steering vector on k is omitted in notation)

$$\mathbf{v}(r_l, \Psi_l) = \left[\frac{e^{-ik\|\mathbf{r}_1 - \mathbf{r}_l\|}}{\|\mathbf{r}_1 - \mathbf{r}_l\|}, \frac{e^{-ik\|\mathbf{r}_2 - \mathbf{r}_l\|}}{\|\mathbf{r}_2 - \mathbf{r}_l\|}, \dots, \frac{e^{-ik\|\mathbf{r}_Q - \mathbf{r}_l\|}}{\|\mathbf{r}_Q - \mathbf{r}_l\|} \right]^T. \quad (25)$$

The signal model in (23) is the near-field spatial domain array signal model. We next develop the signal model in the S²H domain.

Each term in the steering vector represents a unit-amplitude spherical wave, and hence, we can use (14) to represent the steering vector (and by extension the steering matrix) in the

S^2H domain. Truncating the summation in (14) to order N (where N is referred to as the array order), each term in the steering vector can be written as

$$\frac{e^{-ik\|\mathbf{r}_q - \mathbf{r}_l\|}}{\|\mathbf{r}_q - \mathbf{r}_l\|} = \sum_{n=0}^N \sum_{m=-n}^n \tilde{b}_n(k, r_l, r_a) [T_n^m(\Psi_l)]^* T_n^m(\Phi_q). \quad (26)$$

Then, we can express the steering matrix as

$$\mathbf{V}(r, \Psi) = \mathbf{T}(\Phi) [\mathcal{B}(r_1) \mathbf{t}^H(\Psi_1), \dots, \mathcal{B}(r_L) \mathbf{t}^H(\Psi_L)], \quad (27)$$

where $\mathbf{T}(\Phi)$ is a $Q \times (N+1)^2$ sized matrix whose q^{th} row is expressed as

$$\mathbf{t}(\Phi_q) = [T_0^0(\Phi_q), T_1^{-1}(\Phi_q), T_1^0(\Phi_q), T_1^1(\Phi_q), \dots, T_N^N(\Phi_q)]. \quad (28)$$

$\mathbf{t}(\Psi_l)$ is a $1 \times (N+1)^2$ row vector which is defined in the same way as (28) with Φ_q replaced by Ψ_l . $\mathcal{B}(r_l)$ is a diagonal matrix of size $(N+1)^2 \times (N+1)^2$ and is expressed as

$$\mathcal{B}(r_l) = \text{diag}(\tilde{b}_0(k, r_l, r_a), \tilde{b}_1(k, r_l, r_a), \tilde{b}_1(k, r_l, r_a), \dots, \tilde{b}_n(k, r_l, r_a)). \quad (29)$$

The dependence of $\mathcal{B}(r_l)$ on r_a and k is omitted for notational brevity. If the pressure were continuously observed over the entire spherical sector, then the S^2H transformation of the pressure would be obtained by the integral in (4). However, in our case, the spherical sector microphone array only samples the pressure field at discrete spatial locations over the sector. Hence, in practical cases, the S^2H transform of the pressure field is approximated by a summation as

$$P_{nm}(k, r) \approx \sum_{q=1}^Q \gamma_q P_q(k) [T_n^m(\Phi_q)]^*. \quad (30)$$

where γ_q is the q^{th} microphone's sampling weight. The weights are usually chosen based on various sampling schemes as presented in [39]. Now, for all $0 \leq n \leq N$ and $-n \leq m \leq n$, the S^2H transform in (30) can be written in a matrix form as

$$\mathbf{P}_{nm}(k, r) \approx \mathbf{T}^H(\Phi) \mathbf{\Gamma} \mathbf{P}(k), \quad (31)$$

where $\mathbf{\Gamma} = \text{diag}(\gamma_1, \gamma_2, \dots, \gamma_Q)$ and $\mathbf{P}_{nm} = [P_{00}, P_{1(-1)}, P_{10}, P_{11}, \dots, P_{NN}]^T$. Using the orthonormality condition of the S^2H basis function, the following condition holds

$$\mathbf{T}^H(\Phi) \mathbf{\Gamma} \mathbf{T}(\Phi) = \mathbf{I}_{(N+1)^2}, \quad (32)$$

where $\mathbf{I}_{(N+1)^2}$ is an identity matrix of size $(N+1)^2 \times (N+1)^2$. Now, substituting (27) into the array signal model (23) and left-multiplying both sides by $\mathbf{T}^H(\Phi) \mathbf{\Gamma}$, we can write the near-field data model in the S^2H domain as

$$\mathbf{P}_{nm}(k) = [\mathcal{B}(r_1) \mathbf{t}^H(\Psi_1), \dots, \mathcal{B}(r_L) \mathbf{t}^H(\Psi_L)] \mathbf{S}(k) + \mathbf{G}_{nm}(k), \quad (33)$$

where $\mathbf{G}_{nm}(k) = \mathbf{T}^H(\Phi) \mathbf{\Gamma} \mathbf{G}(k)$. We can write the array model in (33) in a compact manner as

$$\mathbf{P}_{nm}(k) = \mathbf{V}_{nm}(r, \Psi) \mathbf{S}(k) + \mathbf{G}_{nm}(k), \quad (34)$$

where $\mathbf{V}_{nm}(r, \Psi)$ is the near-field steering matrix in the S^2H domain and is expressed as

$$\mathbf{V}_{nm}(r, \Psi) = [\mathcal{B}(r_1) \mathbf{t}^H(\Psi_1), \dots, \mathcal{B}(r_L) \mathbf{t}^H(\Psi_L)]. \quad (35)$$

In the next section, we propose our near-field localization techniques based on the array signal model in (34).

IV. PROPOSED LOCALIZATION OF NEAR-FIELD SOURCES USING SPHERICAL SECTOR MICROPHONE ARRAY

The steering vector of a near-field source located at $\mathbf{r} = (r, \Psi)$ in the S^2H domain, based on the array model in (34), can be expressed as

$$\mathbf{v}_{nm}(r, \Psi) = \mathcal{B}(r) \mathbf{t}^H(\Psi). \quad (36)$$

We can see the separation in the radial and angular components of the steering vector in the S^2H domain. This should lead to better range and angular estimation of the near-field source than the spatial domain steering vector in (25). Also, from the representation of mode strength in (16), it is much easier to model scattering from the surface of a rigid spherical sector array in the S^2H domain than the spatial domain. We now present near-field localization techniques for jointly estimating the range, elevation and azimuth locations of the source in the S^2H domain. The range has to be searched over r as in (18) and Ψ has to be searched over $\theta_1 \leq \theta \leq \theta_2$ and $\phi_1 \leq \phi \leq \phi_2$.

A. Spherical Sector Harmonics MUSIC for Near-Field Localization (NF- S^2H -MUSIC)

MUSIC is a subspace-based algorithm wherein we need the covariance matrix of the array signal to obtain the noise subspace. For our model, the array covariance matrix can be expressed as

$$\mathbf{R}_{\mathbf{P}_{nm}} = \mathbb{E}[\mathbf{P}_{nm}(k) \mathbf{P}_{nm}^H(k)]. \quad (37)$$

In practical situations with limited snapshots, the covariance matrix is estimated using the sample covariance matrix as $\hat{\mathbf{R}}_{\mathbf{P}_{nm}} = \frac{1}{N_s} \sum_{\nu=1}^{N_s} \mathbf{P}_{nm}(k_\nu) \mathbf{P}_{nm}^H(k_\nu)$. The proposed NF- S^2H -MUSIC magnitude spectrum is now calculated as

$$D_{\text{NF-}S^2H\text{-MUSIC}}(r, \Psi) = \frac{1}{\mathbf{v}_{nm}^H(r, \Psi) \mathbf{U}_{nm} \mathbf{U}_{nm}^H \mathbf{v}_{nm}(r, \Psi)}, \quad (38)$$

where \mathbf{U}_{nm} is the noise subspace of $\hat{\mathbf{R}}_{\mathbf{P}_{nm}}$. The noise subspace is obtained by using the lowest $((N+1)^2 - L)$ eigenvalues of $\hat{\mathbf{R}}_{\mathbf{P}_{nm}}$. The number of sources should satisfy the condition $L < (N+1)^2$. As the steering vectors of the near-field sources are orthogonal to the noise subspace, the denominator of the NF- S^2H -MUSIC spatial spectrum tends to zero whenever (r, Ψ) corresponds to any of the source locations. This means that the NF- S^2H -MUSIC spectrum gives a peak at the locations of the sources.

B. Spherical Sector Harmonics MVDR for Near-Field Localization (NF- S^2H -MVDR)

MVDR is a beamforming based source localization technique that minimizes the interference-plus-noise power while maintaining a distortionless constraint (or a unity gain) towards the

desired source direction. For our case of near-field localization using the array model (34), the proposed NF-S²H-MVDR spectrum is calculated as

$$D_{\text{NF-S}^2\text{H-MVDR}}(r, \Psi) = \frac{1}{\mathbf{v}_{\text{nm}}^H(r, \Psi) \hat{\mathbf{R}}_{\mathbf{P}_{\text{nm}}}^{-1} \mathbf{v}_{\text{nm}}(r, \Psi)}. \quad (39)$$

The NF-S²H-MVDR also gives peaks at the location of L near-field sources. As MVDR can also be used as a beamformer, we develop an MVDR-based near-field beamformer in the S²H domain in Sec. V.

C. Analysis of the Cramer-Rao Bound

In estimation theory, the CRB provides a lower bound on the variance of any unbiased estimator for a parameter in a statistical model. The CRB for DOA estimation of far-field sources and source localization of near-field sources in the SH domain was derived in [40] and [24], respectively. Following the formulation in these two works, we derive the CRB for near-field source localization in the S²H domain in this subsection. The vector of unknown parameters to be estimated is

$$\boldsymbol{\eta} = [r_1, r_2, \dots, r_L, \theta_1, \theta_2, \dots, \theta_L, \phi_1, \phi_2, \dots, \phi_L]^T. \quad (40)$$

The Fisher Information Matrix (FIM) of the parameters is written as

$$\mathcal{M} = \begin{bmatrix} \mathcal{M}_{\mathbf{r}\mathbf{r}} & \mathcal{M}_{\mathbf{r}\boldsymbol{\theta}} & \mathcal{M}_{\mathbf{r}\boldsymbol{\phi}} \\ \mathcal{M}_{\boldsymbol{\theta}\mathbf{r}} & \mathcal{M}_{\boldsymbol{\theta}\boldsymbol{\theta}} & \mathcal{M}_{\boldsymbol{\theta}\boldsymbol{\phi}} \\ \mathcal{M}_{\boldsymbol{\phi}\mathbf{r}} & \mathcal{M}_{\boldsymbol{\phi}\boldsymbol{\theta}} & \mathcal{M}_{\boldsymbol{\phi}\boldsymbol{\phi}} \end{bmatrix}. \quad (41)$$

where $\mathbf{r} = [r_1, r_2, \dots, r_L]^T$, $\boldsymbol{\theta} = [\theta_1, \theta_2, \dots, \theta_L]^T$ and $\boldsymbol{\phi} = [\phi_1, \phi_2, \dots, \phi_L]^T$. The individual blocks of the FIM can be obtained by replacing the far-field steering vector in [40] with the near-field steering vector in (36) as

$$\begin{aligned} \mathcal{M}_{\mathbf{r}\boldsymbol{\theta}} &= 2\text{Re} \{ (\mathbf{R}_S \mathbf{V}_{\text{nm}}^H \mathbf{R}_P^{-1} \mathbf{V}_{\text{nm}} \mathbf{R}_S)^T \odot (\bar{\mathbf{V}}_{\text{nm}\mathbf{r}}^H \mathbf{R}_P^{-1} \bar{\mathbf{V}}_{\text{nm}\boldsymbol{\theta}}) \\ &\quad + (\mathbf{R}_S \mathbf{V}_{\text{nm}}^H \mathbf{R}_P^{-1} \bar{\mathbf{V}}_{\text{nm}\mathbf{r}})^T \odot (\mathbf{R}_S \mathbf{V}_{\text{nm}}^H \mathbf{R}_P^{-1} \bar{\mathbf{V}}_{\text{nm}\boldsymbol{\theta}}) \}, \end{aligned} \quad (42)$$

$$\begin{aligned} \mathcal{M}_{\boldsymbol{\theta}\boldsymbol{\phi}} &= 2\text{Re} \{ (\mathbf{R}_S \mathbf{V}_{\text{nm}}^H \mathbf{R}_P^{-1} \mathbf{V}_{\text{nm}} \mathbf{R}_S)^T \odot (\bar{\mathbf{V}}_{\text{nm}\boldsymbol{\theta}}^H \mathbf{R}_P^{-1} \bar{\mathbf{V}}_{\text{nm}\boldsymbol{\phi}}) \\ &\quad + (\mathbf{R}_S \mathbf{V}_{\text{nm}}^H \mathbf{R}_P^{-1} \bar{\mathbf{V}}_{\text{nm}\boldsymbol{\theta}})^T \odot (\mathbf{R}_S \mathbf{V}_{\text{nm}}^H \mathbf{R}_P^{-1} \bar{\mathbf{V}}_{\text{nm}\boldsymbol{\phi}}) \}, \end{aligned} \quad (43)$$

where $\bar{\mathbf{V}}_{\text{nm}\mathbf{r}} = \sum_{l=1}^L \bar{\mathbf{V}}_{\text{nm}\mathbf{r}_l}$ and $\bar{\mathbf{V}}_{\text{nm}\mathbf{r}_l} = \frac{\partial \mathbf{V}_{\text{nm}}(r, \Psi)}{\partial r_l}$. $\bar{\mathbf{V}}_{\text{nm}\boldsymbol{\theta}}$ and $\bar{\mathbf{V}}_{\text{nm}\boldsymbol{\phi}}$ are defined similarly. $\mathbf{R}_S = \mathbb{E}[\mathbf{S}(k) \mathbf{S}^H(k)]$. Other blocks in the FIM can be defined by replacing the appropriate parameters in (42) and (43). The derivative of the steering matrix $\mathbf{V}_{\text{nm}}(r, \theta, \phi)$ with respect to r, θ and ϕ is provided in Appendix B. The CRB for the different parameters can finally be obtained as

$$\text{CRB}[\boldsymbol{\eta}]_i = [\mathcal{M}]_{i,i}^{-1}. \quad (44)$$

V. PROPOSED NEAR-FIELD S²H MVDR BEAMFORMER

The location of the desired near-field source can be estimated using the source localization techniques introduced in the previous section. After localization, a beamformer can be steered towards the desired location to increase the gain in that location and suppress the interfering signals from other locations. In this section, we present a near-field beamformer

capable of radial and angular filtering in the S²H domain based on the MVDR principle. Let \mathbf{w}_{nm} be the beamforming filter and $\mathbf{v}_{\text{nm}}(r_l, \Psi_l)$ be the steering vector of the desired source in the S²H domain. Since the array model in (34) is similar to the model in the spatial domain [4], the weights of the near-field MVDR beamformer in the S²H domain can be obtained by solving the following optimization problem analogous to the MVDR beamformer formulation in the spatial domain

$$\min_{\mathbf{w}_{\text{nm}}} \mathbf{w}_{\text{nm}}^H \hat{\mathbf{R}}_{\mathbf{P}_{\text{nm}}} \mathbf{w}_{\text{nm}} \quad \text{s.t.} \quad \mathbf{w}_{\text{nm}}^H \mathbf{v}_{\text{nm}}(r_l, \Psi_l) = 1. \quad (45)$$

The objective function of the beamformer minimizes the power of the beamformer output, while the constraint puts a unity gain towards the desired location. The solution of (45) is obtained as

$$\mathbf{w}_{\text{nm}} = \frac{\hat{\mathbf{R}}_{\mathbf{P}_{\text{nm}}}^{-1} \mathbf{v}_{\text{nm}}(r_l, \Psi_l)}{\mathbf{v}_{\text{nm}}^H(r_l, \Psi_l) \hat{\mathbf{R}}_{\mathbf{P}_{\text{nm}}}^{-1} \mathbf{v}_{\text{nm}}(r_l, \Psi_l)} \quad (46)$$

For every possible spatial location (r, Ψ) , the beampattern of the near-field MVDR beamformer can now be obtained as

$$\mathcal{Z}(r, \Psi) = |\mathbf{w}_{\text{nm}}^H \mathbf{v}_{\text{nm}}(r, \Psi)|. \quad (47)$$

Once again, the radial range of the beampattern is given by (18) and the angular range is $\theta_1 \leq \theta \leq \theta_2$ and $\phi_1 \leq \phi \leq \phi_2$.

In all our proposed algorithms, we have assumed that the source is present in the same angular sector as the array. In Appendix A, we present a formulation for cases where the source is not restricted to the same angular sector as the array and can be present anywhere.

VI. SIMULATION PERFORMANCE

In this section, we perform various near-field simulations to analyze the performance of the proposed algorithms. Unless otherwise mentioned, for all the simulations, we consider a rigid spherical sector microphone array (S²MA) with 20 microphones placed on a sector given by $\alpha_1 = 2, \alpha_2 = -1$ and $\beta = 1$ with radius $r_a = 0.042m$. This corresponds to a hemispherical sector with an elevation range of $[0^\circ, 90^\circ]$ and an azimuth range of $[0^\circ, 360^\circ]$. The array is capable of capturing a wavefield of order $N = 3$. The 20 microphones are placed at angular locations $\Phi = \{(14.3^\circ, 346.6^\circ), (16.7^\circ, 167.2^\circ), (32.2^\circ, 248^\circ), (33.3^\circ, 85.3^\circ), (45.2^\circ, 39.6^\circ), (45.3^\circ, 350^\circ), (45.8^\circ, 143.6^\circ),$

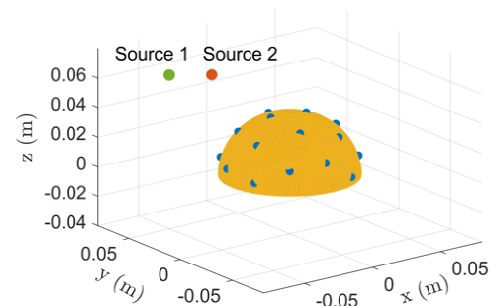


Fig. 4. A spherical sector microphone array ($\alpha_1 = 2, \alpha_2 = -1, \beta = 1$) with 20 microphones and a radius of $r_a = 0.042m$. Two near-field sources are placed at locations $\mathbf{r}_1 = (0.08m, 35^\circ, 135^\circ)$ and $\mathbf{r}_2 = (0.1m, 45^\circ, 150^\circ)$.

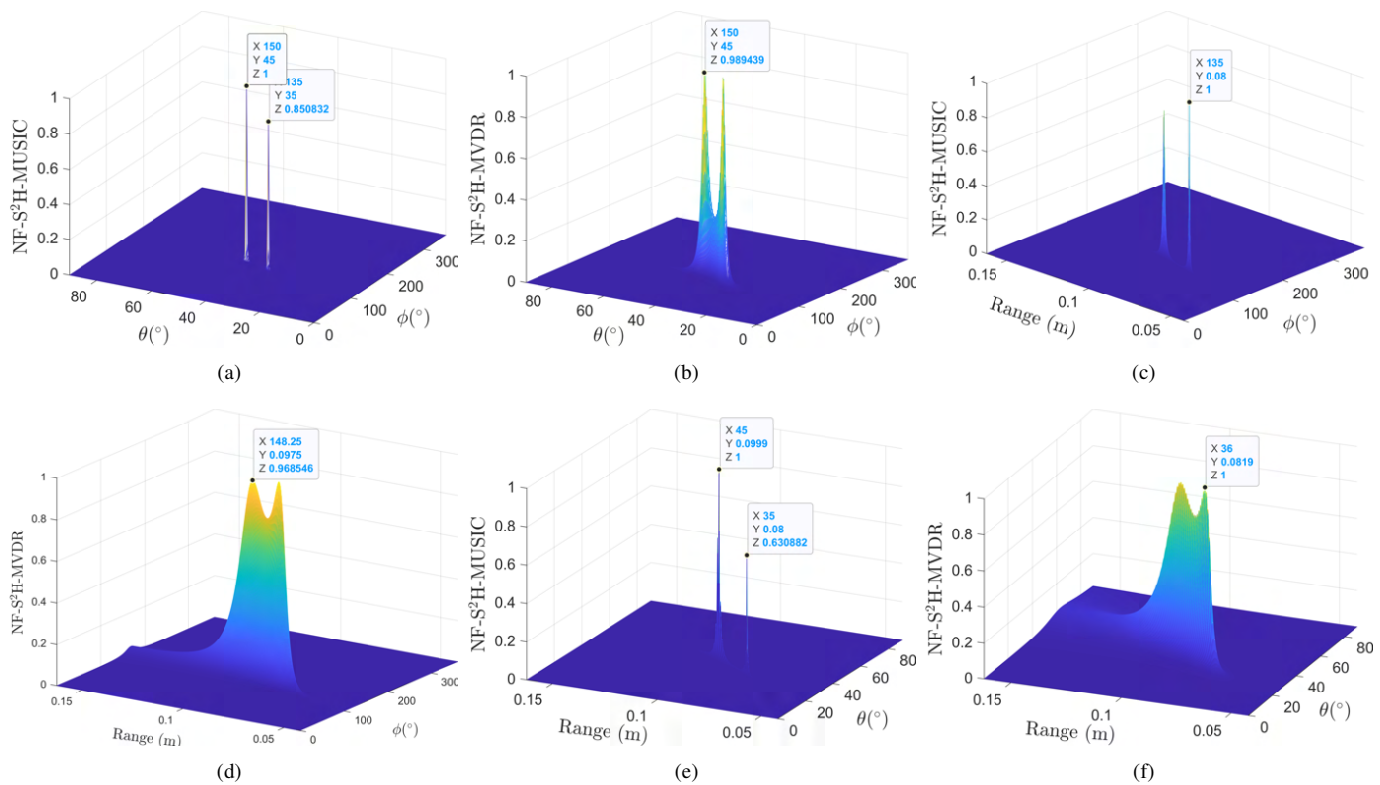


Fig. 5. Magnitude of the spatial spectrum of (a) NF-S²H-MUSIC and (b) NF-S²H-MVDR at fixed range; (c) NF-S²H-MUSIC and (d) NF-S²H-MVDR at fixed elevation & (e) NF-S²H-MUSIC and (f) NF-S²H-MVDR at fixed azimuth. Two near-field sources are present at (0.08m, 35°, 135°) and (0.1m, 45°, 150°).

(46.1°, 302.6°), (47.5°, 195.1°), (61.9°, 100.4°), (63°, 266.6°), (67.4°, 232.6°), (72.4°, 8.0°), (74°, 329.5°), (74.9°, 47.5°), (75.7°, 169.1°), (75.9°, 134.6°), (80.2°, 203°), (81.9°, 292.6°) and (83.4°, 77.5°)}, as shown in Fig. 4. The microphone locations (sampling points) follow a nearly uniform sampling scheme [41], [42] that attempt to distribute the sampling points in a nearly uniform manner on the surface of the spherical sector. In all the simulations, additive white Gaussian noise with adjusted power is used to achieve the desired signal-to-noise ratios (SNRs). The sources will be present in the same angular sector as the array in all simulations unless stated otherwise.

A. Spatial Spectrum of the Proposed Source Localization Methods

We place two closely spaced near-field sources at $\mathbf{r}_1 = (0.08m, 35^\circ, 135^\circ)$ and $\mathbf{r}_2 = (0.1m, 45^\circ, 150^\circ)$ that are emitting spherical waves onto the spherical sector array, as shown in Fig. 4. The frequency of the two signals is 1 kHz and the SNR is set to 5 dB. We now apply NF-S²H-MUSIC and NF-S²H-MVDR to jointly estimate the range, elevation and azimuth locations of both sources. Fig. 5 shows the magnitude of the spatial spectrum of both algorithms. Fig. 5(a) and (b) show the elevation and azimuth plot for a fixed range. We can see that both algorithms show a peak at the location of the two sources. NF-S²H-MUSIC, being a subspace-based algorithm, has a better resolution than NF-S²H-MVDR. Fig. 5(c) and (d) show the range and azimuth plot for a fixed elevation, and once again, both algorithms show peaks at the desired location. The

lower resolution of NF-S²H-MVDR is more clearly visible in the case of range estimation when compared to the high-resolution plot of NF-S²H-MUSIC. Similar conclusions can be drawn from Fig. 5(e) and (f), which show the range and elevation plot for a fixed azimuth.

B. CRB Plots

In this subsection, we plot the CRB for near-field range, elevation and azimuth estimation. We consider two different spherical sector arrays. Sector 1 is the same as described before and sector 2 is given as $\alpha_1 = 2, \alpha_2 = -1$ and $\beta = 3$ (i.e. $\theta \in [0^\circ, 90^\circ]$ and $\phi \in [0^\circ, 120^\circ]$). Both sectors are of radius 0.042m and have 20 microphones. The number of microphones is kept the same so that both sector arrays have the same array order. We assume a single source is placed at (0.085m, 40°, 30°). Fig. 6 shows the CRB for range estimation for different frequencies. The figure shows that the CRB for sector 1 is lower than sector 2 whereas the CRB for $f = 1500$

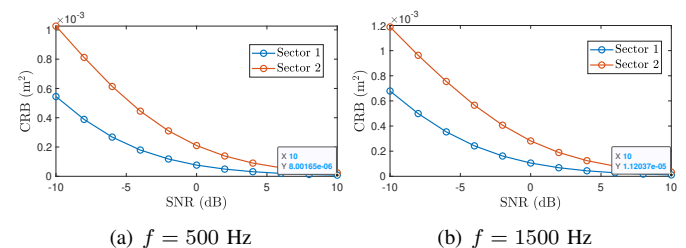


Fig. 6. CRB for range estimation using two different spherical sector arrays.

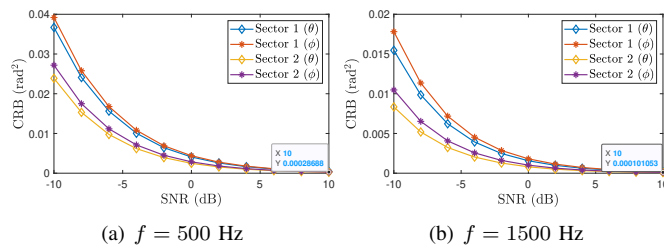


Fig. 7. CRB for elevation and azimuth estimation using two different spherical sector arrays.

Hz is higher than for $f = 500$ Hz. This indicates that a larger sector leads to lower CRB, and a lower frequency leads to lower CRB for near-field range estimation. This is because as frequency increases, the near-field extent of the spherical sector array reduces and the source moves away from the near-field zone to the far-field zone, making range estimation difficult. Fig. 7 shows the CRB for elevation and azimuth estimation for different frequencies. The figure shows that the CRB for sector 1 is higher than sector 2 whereas the CRB for $f = 1500$ Hz is lower than for $f = 500$ Hz for elevation and azimuth estimation, which is the opposite of the behaviour of CRB for range estimation.

C. RMSE Performance of Range, Elevation and Azimuth Estimation

Here, we evaluate the root mean square error (RMSE) performance of the proposed localization algorithms. RMSE for range estimation is calculated as

$$\text{RMSE} = \sqrt{\frac{1}{ZL} \sum_{z=1}^Z \sum_{l=1}^L (\hat{r}_{l,z} - r_l)^2}$$
, where $\hat{r}_{l,z}$ is the estimated range of the l^{th} source in the z^{th} trial and Z is the total number of trials. The RMSE for elevation and azimuth estimation is defined likewise. To obtain the RMSE for range, elevation and azimuth estimation, we consider two sources at $(0.08m, 35^\circ, 150^\circ)$ and $(0.12m, 55^\circ, 170^\circ)$ with a frequency of $f = 500$ Hz. We compare the performances of the proposed algorithms with the baseline spatial domain (SD) MUSIC and MVDR algorithms for near-field sources. We refer to them as NF-SD-MUSIC and NF-SD-MVDR. The SD algorithms use the signal model in (23), whereas the proposed methods use the S²H signal model in (34). Fig. 8 shows the RMSE values averaged over $Z = 200$ trials for different SNRs and number of snapshots (N_s) of all the algorithms, along with the CRB values. From the table, we see that NF-S²H-MUSIC outperforms NF-S²H-MVDR in near-field localization performance as expected. The proposed algorithms in the S²H domain outperform their spatial domain counterparts for both range as well as angular estimation. This may be because of the separation of the radial and angular components of the steering vector in the S²H domain. This allows the proposed S²H domain algorithms to estimate the range and angular components separately, leading to better accuracy than the combined estimation in the spatial domain. MVDR algorithm in both S²H and spatial domain struggle to estimate the range in low snapshot scenarios, with NF-S²H-MVDR outperforming NF-SD-MVDR in such scenarios. Also, since we are using a rigid sector array, the better modelling of scattering in the S²H domain may

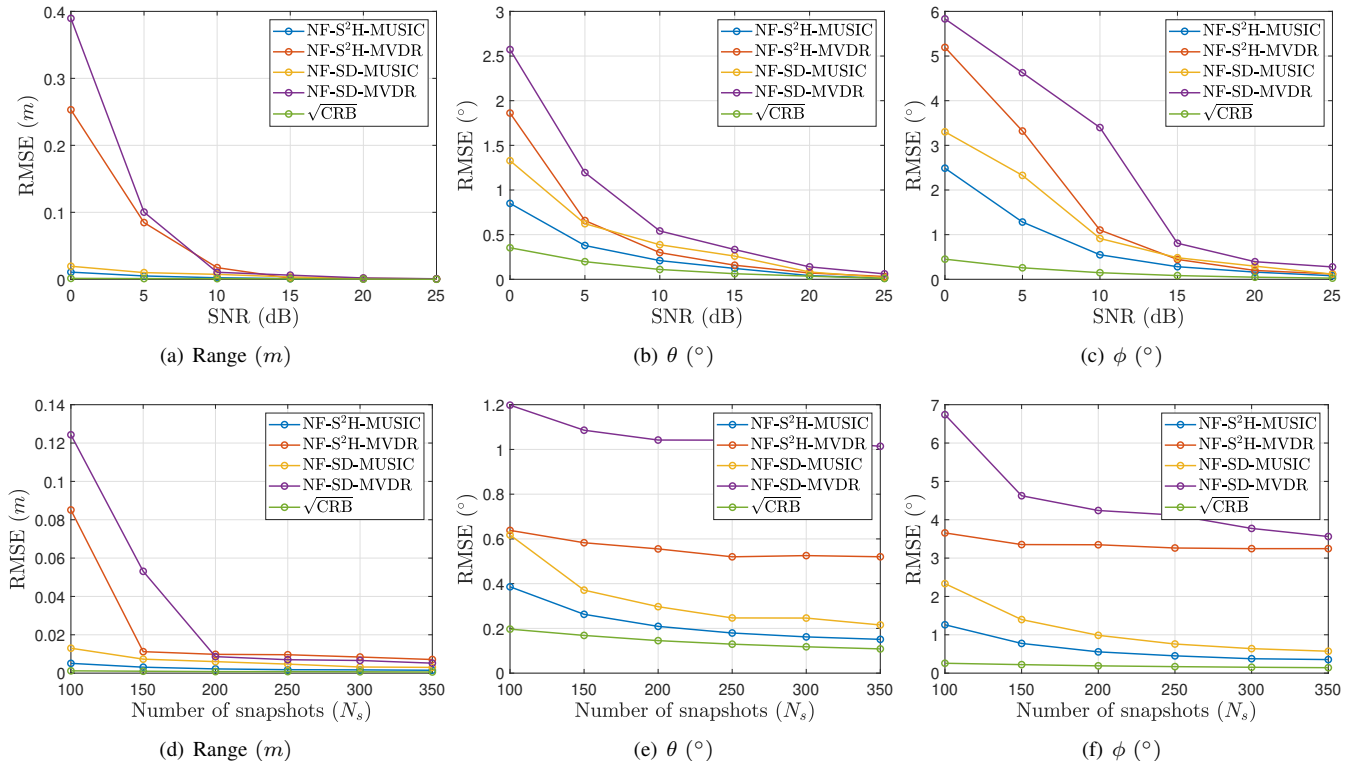


Fig. 8. RMSE of range, elevation and azimuth estimation of the proposed S²H domain algorithms along with a comparison with the baseline spatial domain algorithms and the CRB (the sector array used is shown in Fig. 4).

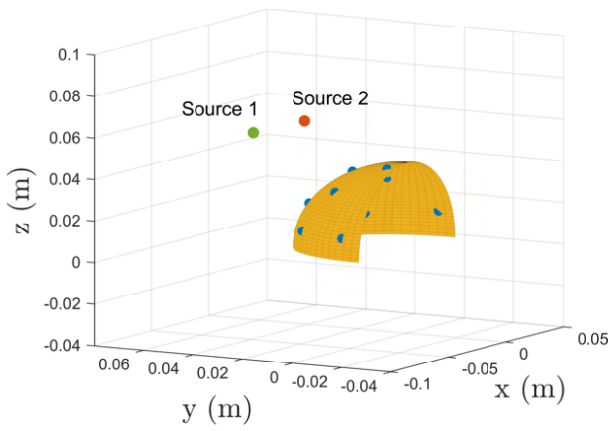


Fig. 9. A spherical sector microphone array ($\alpha_1 = 2, \alpha_2 = -1, \beta = 2$) with 10 microphones and a radius of $r_a = 0.042m$. Two near-field sources are placed at locations $\mathbf{r}_1 = (0.08m, 35^\circ, 150^\circ)$ and $\mathbf{r}_2 = (0.12m, 55^\circ, 170^\circ)$.

TABLE I
RMSE OF RANGE, ELEVATION AND AZIMUTH ESTIMATION USING NF-S²H-MUSIC FOR THE SECTOR ARRAY SHOWN IN FIG. 9.

	SNR ($N_s = 100$)					
	0 dB	5 dB	10 dB	15 dB	20 dB	25 dB
$r(m)$	0.0143	0.0058	0.0028	0.0015	0.0008	0.0004
$\theta (^\circ)$	0.8816	0.4138	0.2229	0.1343	0.0637	0.0134
$\phi (^\circ)$	2.8922	1.4890	0.7360	0.3409	0.2139	0.1334
	Number of snapshots (SNR = 5 dB)					
	100	150	200	250	300	350
$r(m)$	0.0056	0.0038	0.0030	0.0025	0.0022	0.0021
$\theta (^\circ)$	0.4143	0.2811	0.2256	0.2057	0.1824	0.1802
$\phi (^\circ)$	1.5283	0.9636	0.7502	0.6001	0.5383	0.4884

improve the performances of the proposed algorithms in the S²H domain.

We now analyze the RMSE by keeping the source locations and frequency of operation the same but changing the sector array. We use the S²MA shown in Fig. 9. The array order of this sector array is 2. The corresponding RMSE is presented in Table I. Due to the smaller sector size and array order, the RMSE deteriorates when compared to Fig. 8. The drop in performance of NF-S²H-MUSIC is not massive, indicating that when space is a constraint, the smaller sector can be used as long as the trade-off with RMSE performance is within an acceptable limit. The behaviour of other algorithms is expected to show a similar trend.

It is also interesting to note that the CRB plots in Fig. 6 and 7 show that if the number of elements is the same, a smaller sector leads to better angular estimation, and a larger sector leads to better range estimation (as long as the near-field sources are in the same angular sector as the array). However, since the array in Fig. 9 has half the number of elements than the array in Fig. 4, the RMSE increases for all range, elevation and azimuth estimation using the smaller sector array.

D. Probability of Resolution of Range Estimation

To evaluate the probability of resolution, we assume two near-field sources close to each other with the same azimuth and el-

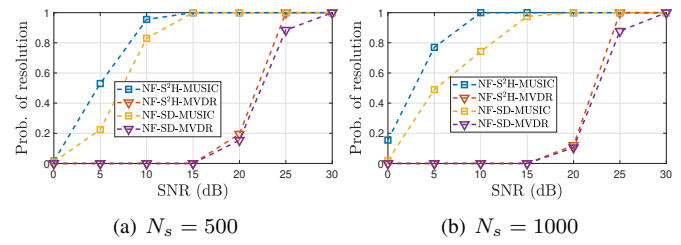


Fig. 10. Probability of resolution for range estimation of the proposed algorithms and the baseline spatial domain algorithms with varying SNRs.

evaluation angle at $(0.065m, 40^\circ, 165^\circ)$ and $(0.095m, 40^\circ, 165^\circ)$ from the S²MA shown in Fig. 4. The frequency of operation is 220 Hz. The probability of resolution (PR) is defined as the ratio of successful range estimation of both sources to the total number of trials. Range estimation is considered a success if the condition $|\hat{r}_{l,z} - r_l| < 0.005m$ is satisfied for both the sources. Fig. 10 shows the PR for both the proposed and the baseline spatial domain localization algorithms for varying SNRs and two different number of snapshots. The figure shows that PR improves with increasing SNR and number of snapshots and that the S²H domain algorithms perform better than the spatial domain algorithms. The figure once again highlights the better resolution capability of NF-S²H-MUSIC over NF-S²H-MVDR as the latter is unable to resolve the sources for lower SNRs.

E. Beampattern Analysis of Near-Field S²H MVDR Beamformer

To analyze the beampattern of the proposed beamformer in Sec. V, we place two near-field sources at locations given by source 1: $(0.1m, 30^\circ, 50^\circ)$ and source 2: $(0.3m, 40^\circ, 70^\circ)$. The frequency of operation is considered to be 500 Hz and the SNR is fixed at 10 dB. Source 2 is considered to be the desired source and source 1 is the interfering source. The beampattern obtained from (47) is plotted in Fig. 11. Fig. 11(a) shows the beampattern for elevation and azimuth with a fixed range. The figure shows that the array gain in the desired direction is 0.84 dB while the gain towards the interfering direction is -50.98 dB. Fig. 11(b) shows the beampattern for range and azimuth with fixed elevation. The gain at the desired location is almost -1.22 dB (close to unity gain), while the gain at the interfering source location is approximately -27.54 dB. Thus, the proposed beamformer is capable of both radial as well as angular spatial filtering.

Fig. 12 shows the 2D version of Fig. 11. Fig. 12(a) and (b) show the beampattern for different azimuth angles at the undesired range of $r = 0.1m$ and the desired range of $r = 0.3m$ for a fixed elevation, respectively. From Fig. 12(a), the array gain is much lower at the azimuth angle of source 1 than source 2 as desired. From Fig. 12(b), there is no sudden drop in the array gain around the undesired azimuth angle. Fig. 12(c) and (d) show the beampattern for different ranges at the undesired azimuth of $\phi = 50^\circ$ and the desired azimuth of $\phi = 70^\circ$ for a fixed elevation, respectively. From Fig. 12(c), the array gain is much lower at the range of source 1 than source 2 as desired. From Fig. 12(d), there is a drop in the array gain

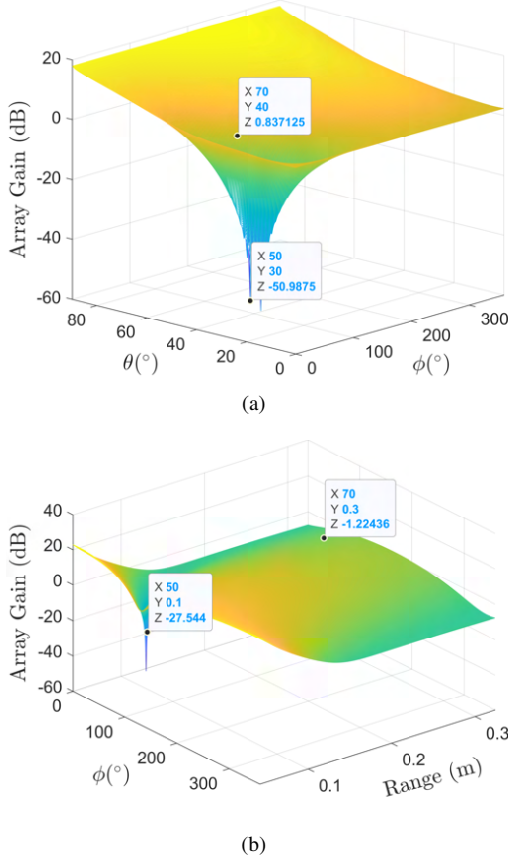


Fig. 11. Beampattern of the proposed near-field S²H MVDR beamformer with the desired source present at $(0.3m, 40^\circ, 70^\circ)$ and the interfering source present at $(0.1m, 30^\circ, 50^\circ)$.

around the undesired range. So, from Fig. 12(a) and (c), the beamformer filters out the signal coming from the undesired location. And from Fig. 12(b) and (d), we can conclude that the beamformer is more sensitive to radial variation than azimuth variation around the desired location. This can be beneficial in

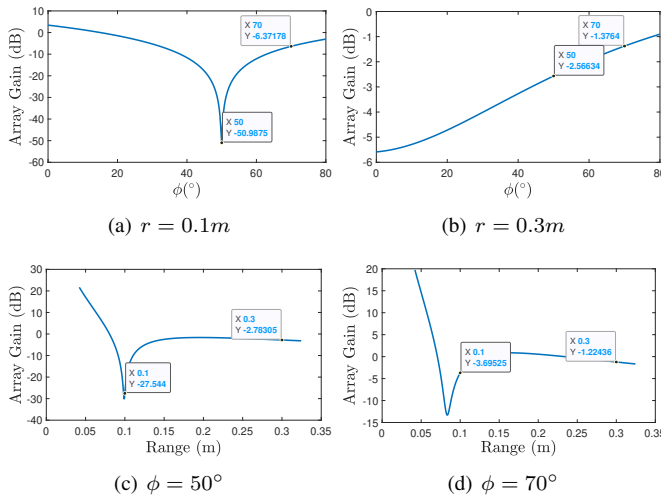


Fig. 12. 2D beampattern of the proposed near-field S²H MVDR beamformer with the desired source present at $(0.3m, 40^\circ, 70^\circ)$ and the interfering source present at $(0.1m, 30^\circ, 50^\circ)$.

applications where a slight variation in the azimuth direction of the desired source is anticipated.

F. Performance of Near-Field Localization with Increasing Range of the Source

In this subsection, we analyse the performance of the proposed near-field source localization methods as the source moves further away from the array. A single source is considered with direction $(40^\circ, 60^\circ)$ with a frequency of 1500 kHz. For this frequency with $N = 3$ and $r_a = 0.042m$, the near-field range is $0.042m \leq r_l \leq 0.108m$. We plot the spatial spectrum of NF-S²H-MUSIC and NF-S²H-MVDR for three values of $r_l = 0.06m, 0.1m$ and $0.7m$. All the spatial spectrum plots are shown in Fig. 13. Since $r_l = 0.06m$ is closest to the array and well within the near-field range, the spectrum in Fig. (a) and (b) for both NF-S²H-MUSIC and NF-S²H-MVDR give a precise and narrow peak at the source location. For $r_l = 0.1m$, which is at the near-field border, the width of the peak is still narrow for NF-S²H-MUSIC while the peak for NF-S²H-MVDR becomes broader. Finally, for $r_l = 0.7m$, which is outside the near-field range, the peak of NF-S²H-MUSIC broadens while the spectrum of NF-S²H-MVDR is unusable. Thus, the near-field methods degrade

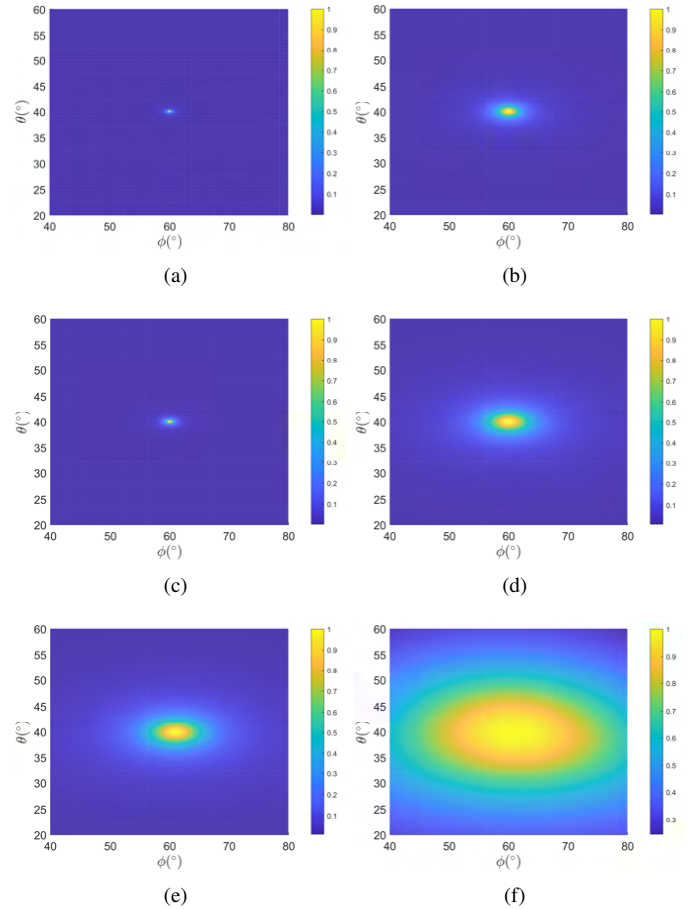


Fig. 13. Spatial spectrum of NF-S²H-MUSIC (first column) and NF-S²H-MVDR (second column) as the source moves away from the array. Both algorithms localize the source better in the near-field as seen in (a) and (b) than in the far-field as seen in (e) and (f), respectively.

TABLE II
COMPUTATIONAL COMPLEXITY ANALYSIS OF THE PROPOSED NEAR FIELD S²H ALGORITHMS AND SPATIAL DOMAIN BASED ALGORITHMS

	Multiplications (\times)	Additions (+)	Divisions (/)	Matrix Inverse
NF-S ² H-MUSIC	$[(N+1)^2 + 1]QN_s + (N+1)^4N_s + \mathcal{O}[(N+1)^6] + G[(N+1)^2 + 1)((N+1)^2 - L)]$	$(N+1)^2(Q-1)N_s + (N+1)^4(N_s-1) + \mathcal{O}[(N+1)^6] + G[(N+1)^2((N+1)^2 - L) - 1]$	$(N+1)^2N_s + G$	-
NF-S ² H-MVDR	$[(N+1)^2 + 1]QN_s + (N+1)^4N_s + 2(N+1)^4$	$(N+1)^2(Q-1)N_s + (N+1)^4(N_s-1) + 2(N+1)^2((N+1)^2 - 1)$	$(N+1)^2N_s + G$	$\mathcal{O}[(N+1)^6]$
NF-SD-MUSIC	$Q^2N_s + \mathcal{O}[Q^3] + G[(Q+1)(Q-L)]$	$Q^2(N_s-1) + \mathcal{O}(Q^3) + G[Q(Q-L) - 1]$	$QN_s + G$	-
NF-SD-MVDR	$Q^2N_s + 2Q^2$	$Q^2(N_s-1) + 2Q(Q-1)$	$QN_s + G$	$\mathcal{O}[Q^3]$

* G is the total number of grid points at which the magnitude spectrum of all the algorithms is calculated.

in performance in the far-field region. Fig. 13 also again highlights the difference in resolution of the NF-S²H-MUSIC and NF-S²H-MVDR methods.

G. Computational Complexity Analysis

Finally, we analyze the computational complexity of the proposed S²H algorithms in terms of the total number of complex multiplications, additions, divisions and matrix inversion needed and compare them with the SD algorithms. The complexity is shown in Table II. The most computationally expensive step for the MUSIC algorithm is the eigenvalue decomposition (EVD). In this step, the dimensionality reduction in the S²H domain leads to lower complexity than the spatial domain algorithm as $(N+1)^2 < Q$. For the MVDR algorithm, the inversion of the array covariance matrix is the most computationally expensive step. Again, in this step, the proposed NF-S²H-MVDR is more computationally efficient than the NF-SD-MVDR due to the dimensionality reduction. Even in the other steps, such as calculating the covariance matrix or calculating the magnitude spectrum, the proposed S²H domain algorithms need lower computations when compared to the spatial domain algorithms. The extra

TABLE III
RUN TIME AND RESOURCE REQUIREMENT OF THE PROPOSED AND SPATIAL DOMAIN ALGORITHMS

	Run Time (s)	CPU (%)	Memory usage (MB)
NF-S ² H-MUSIC	6.3727	29.57	2522.1
NF-S ² H-MVDR	5.2707	25.34	2486.2
NF-SD-MUSIC	7.2171	31.82	2715.2
NF-SD-MVDR	5.9348	28.16	2504.3

computational step in the proposed algorithms corresponds to the transformation of the array data to the S²H domain.

We also tabulate the computational time and resources required by the proposed localization algorithms and compare them with the spatial domain algorithms in Table III. The algorithms were run on a system with an Intel(R) Core(TM) i5-9500 CPU with a clock frequency of 3 GHz and 20 GB of RAM. The run times of the algorithm were calculated using the *tic* and *toc* functions in MATLAB version R2021b. The memory requirement and CPU usage were obtained through Microsoft Windows' system information app [43]. The acoustic scenario laid out in VI-A was considered. From

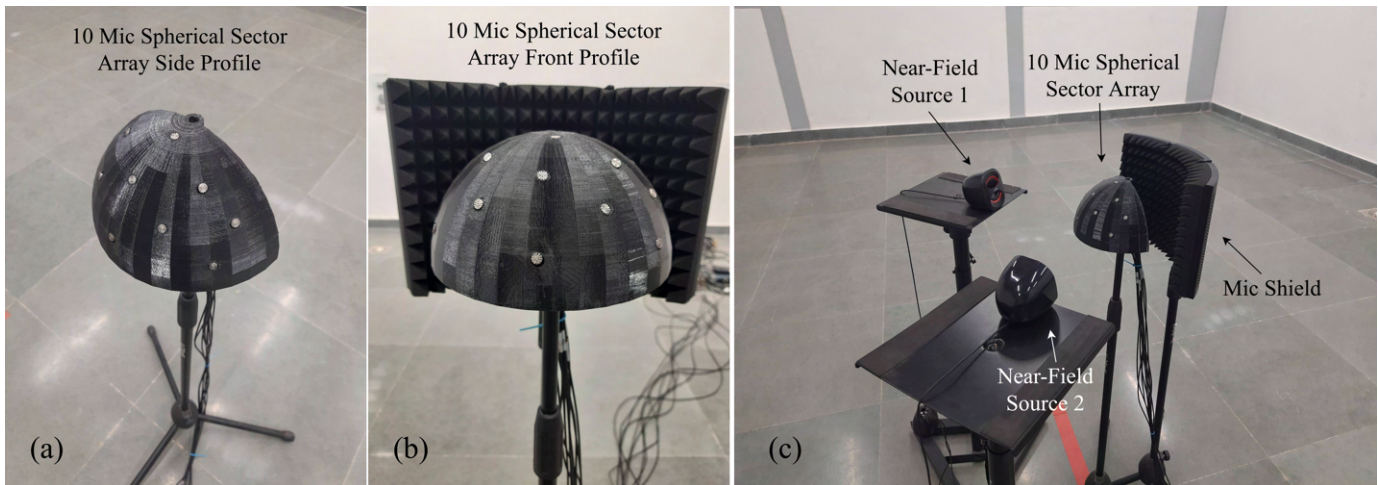


Fig. 14. The experimental setup for localization two near-field sources with a spherical sector microphone array ($\alpha_1 = 2, \alpha_2 = -1, \beta = 2$) using our proposed NF-S²H-MUSIC and NF-S²H-MVDR algorithms. (a) The side profile of the sector array. (b) The front profile of the sector array with the mic shield. (c) The entire setup showing two near-field sources, the sector array and a mic shield.

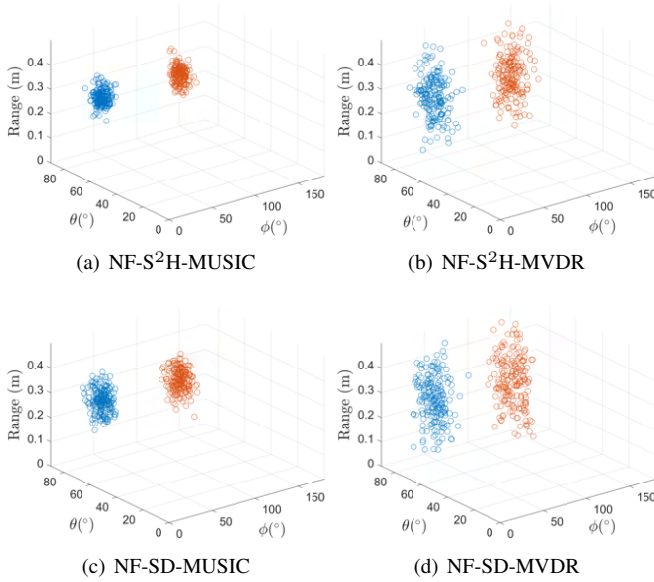


Fig. 15. Scatter plots of 200 trials showing the performance of near-field localization of various algorithms for the experimental setup in Fig. 14

the table, as expected from the computational complexity analysis, NF-SD-MUSIC and NF-SD-MVDR need more time and resources than the proposed NF-S²H-MUSIC and NF-S²H-MVDR algorithms, respectively. Also, NF-S²H-MVDR is slightly less time and resource consuming than NF-S²H-MUSIC. However, it is to be noted that NF-S²H-MUSIC performs significantly better, especially in range estimation.

VII. EXPERIMENTAL EVALUATION

In this section, we test the performance of the proposed algorithms in a real-world setting. The experimental setup is shown in Fig. 14. A spherical sector microphone array ($\alpha_1 = 2, \alpha_2 = -1, \beta = 2$) with 10 microphones and a radius of 10 cm is placed at the center of the x-y plane of a rectangular room of dimension $10 \times 6 \times 5 \text{ m}^3$. The center of the spherical sector is considered to be the origin. GRAS® 40PL-10 CCP free-field array microphones are used. Two near field sources are placed at a distance of 0.25m from the array. The elevation angle of both the sources is 80° . And the azimuth angles of the first and second sources are 45° and 135° , respectively. The sources were emitting a monotone of frequency 300 Hz.

Although the direct-to-reverberation ratio (DRR) of near-field sources is usually high, we used a mic shield to reduce the effect of reverberation in a passive manner in our experimental setup. To further remove reverberation, we used the weighted prediction error (WPE) method [44] in time domain before implementing all the localization algorithms. To obtain the reverberation time from the location of the near-field sources to the microphones, we made use of sine sweeps to measure the room impulse responses.

The results of experiment are shown in Fig. 15 for 200 trials of the experiment. From the figure, we can see that proposed NF-S²H-MUSIC performs the best. The two MVDR algorithms struggle with the range estimation as the points are

TABLE IV
RMSE FOR THE 200 TRIAL RUNS OF THE EXPERIMENT

	$r(m)$	$\theta(^\circ)$	$\phi(^\circ)$
NF-S²H-MUSIC	0.0318	3.6615	4.1311
NF-S²H-MVDR	0.0922	5.9116	7.5827
NF-SD-MUSIC	0.0446	4.7891	5.2939
NF-SD-MVDR	0.1119	6.8785	8.1110

scattered more along the range axis. The RMSE values of all the algorithms for the 200 trials is tabulated in Table IV. The table confirms the results observed so far in the simulations with NF-S²H-MUSIC outperforming the other algorithms even in a real world setting. The RMSE off all the algorithms is higher than the simulations. This is because of all the non-idealities present in the experimental setup. Some of these non-idealities are - the external diameter of the mini loudspeakers (32 mm) is not a point source, the reflections from the mic stands and the speaker stands, some residual reverberation etc. These practical non-idealities degrade the performance of the algorithms when compared to the simulated performance.

VIII. CONCLUSION

This work introduces near-field acoustic localization and beamforming using a spherical sector microphone (S²MA) array. Unlike a spherical array where microphones are placed over the entire surface of the sphere, in an S²MA, the microphones are placed only in a specific sector of the sphere's surface. This generalizes the design of spherical arrays and makes S²MAs suitable for many applications. We begin our work by first decomposing the spherical waves from near-field sources in the S²H domain using the orthonormal S²H basis functions. Then, using the decomposition, we developed a novel near-field array data model in the S²H domain. Based on the data model, acoustic localization and beamforming techniques are proposed for near-field sources. The CRB for near-field localization in the S²H domain is also presented. Various near-field simulations and an experiment has been performed to highlight the performance of the proposed algorithms. In the future, sparsity-based localization, dereverberation, blind source separation, speech diarization, etc., of near-field sources will be developed in the S²H domain based on the array model presented in this work.

APPENDIX

A. Near-field source not present in the angular sector of the array

We note that due to the presence of the term $T_n^m(\Psi_l)$ in (26), the source is restricted to lie in the same angular as that of the spherical sector array. So, $T_n^m(\Psi_l)$ is an appropriate choice if the source is located in the angular sector of the array. However, if a source is located anywhere other than the sector, then the unit amplitude near-field pressure can be modified as

$$\frac{e^{-ik\|\mathbf{r}_q - \mathbf{r}_l\|}}{\|\mathbf{r}_q - \mathbf{r}_l\|} = \sum_{n=0}^N \sum_{m=-n}^n \ddot{b}_n(k, r_l, r_a) [Y_n^m(\Psi_l)]^* T_n^m(\Phi_q), \quad (48)$$

where $Y_n^m(\Psi_l)$ is the spherical harmonics basis function defined as

$$Y_n^m(\theta, \phi) = \sqrt{\frac{(2n+1)(n-m)!}{4\pi(n+m)!}} \mathcal{P}_n^m(\cos \theta) e^{im\phi}, \quad \forall 0 \leq n \leq N, 0 \leq m \leq n$$

$$= (-1)^{|m|} Y_n^{|m|*}(\theta, \phi), \quad \forall -n \leq m < 0 \quad (49)$$

and the modified n^{th} order strength of the near-field mode $\ddot{b}_n(k, r_l, r_a)$ is related to the modified n^{th} order strength of the far-field mode strength $\ddot{b}_n(k, r_a)$ in the same way as (15)

$$\ddot{b}_n(k, r_l, r_a) = i^{-(n-1)} k \ddot{b}_n(k, r_a) h_n(kr_l), \quad (50)$$

where $\ddot{b}_n(k, r_a)$ is expressed as

$$\ddot{b}_n(k, r) = \begin{cases} \frac{4\pi i^n}{\sqrt{\alpha_1^{(2n+1)}} \beta} j_n(kr) & : \text{open sector} \\ \frac{4\pi i^n}{\sqrt{\alpha_1^{(2n+1)}} \beta} \left(j_n(kr) - \frac{j'_n(kr_a)}{h'_n(kr_a)} h_n(kr) \right) & : \text{rigid sector,} \end{cases} \quad (51)$$

Now, the entire formulation of near-field source localization can be carried out as presented in Section III and IV using the transformation in (48) for the case when the source is not in the same angular sector as the array.

B. Derivative of the S^2H near-field steering vector

We rewrite the near-field steering matrix in the S^2H domain

$$\mathbf{V}_{\text{nm}}(r, \Psi) = [\mathcal{B}(r_1) \mathbf{t}^H(\Psi_1), \dots, \mathcal{B}(r_L) \mathbf{t}^H(\Psi_L)]. \quad (52)$$

We note that only the l^{th} column of $\mathbf{V}_{\text{nm}}(r, \Psi)$ has the parameters (r_l, θ_l, ϕ_l) . So,

$$\frac{\partial \mathbf{V}_{\text{nm}}(r, \Psi)}{\partial r_l} = \left[\mathbf{0}, \mathbf{0}, \dots, \frac{\partial \mathcal{B}(r_l) \mathbf{t}^H(\Psi_l)}{\partial r_l}, \dots, \mathbf{0}, \mathbf{0} \right] \quad (53)$$

The derivative of $\mathcal{B}(r_l)$ with respect to r_l depends on the derivative of $h_n(kr_l)$. To facilitate that, we use the following recursive relations of the spherical Hankel function [24], [38]

$$\frac{2n+1}{x} h_n(x) = h_{n-1}(x) + h_{n+1}(x)$$

$$h'_n(x) = h_{n-1}(x) - \frac{n+1}{x} h_n(x),$$

which leads to

$$h'_n(x) = \frac{n}{x} h_n(x) - h_{n+1}(x). \quad (54)$$

Substituting $x = kr_l$, we finally get

$$\frac{\partial h_n(kr_l)}{\partial r_l} = \frac{n}{r_l} h_n(kr_l) - k h_{n+1}(kr_l). \quad (55)$$

In a similar manner, the derivative of $\mathbf{V}_{\text{nm}}(r, \Psi)$ with respect to θ_l will result in zero columns except at the non-zero l^{th} column $\frac{\partial \mathcal{B}(r_l) \mathbf{t}^H(\Psi_l)}{\partial \theta_l}$, which involves the derivative of the

shifted ALP $\tilde{\mathcal{P}}_n^m(\cos \theta)$. To facilitate that, we use the following recursive relations of ALPs [45]

$$(2n+1)x \mathcal{P}_n^m(x) = (n+m) \mathcal{P}_{n-1}^m(x) + (n-m+1) \mathcal{P}_{n+1}^m(x)$$

$$\frac{\partial \mathcal{P}_n^m(x)}{\partial x} = \frac{1}{x^2-1} [x n \mathcal{P}_n^m(x) - (n+m) \mathcal{P}_{n-1}^m(x)],$$

which leads to

$$\frac{\partial \mathcal{P}_n^m(x)}{\partial x} = \frac{1}{x^2-1} [(n-m+1) \mathcal{P}_{n+1}^m(x) - (n+1)x \mathcal{P}_n^m(x)]. \quad (56)$$

Substituting $x = \alpha_1 \cos \theta + \alpha_2$, we get

$$\frac{\partial \tilde{\mathcal{P}}_n^m(\cos \theta)}{\partial \theta} = \frac{\alpha_1 \sin \theta}{1 - (\alpha_1 \cos \theta + \alpha_2)^2} [(n-m+1) \tilde{\mathcal{P}}_{n+1}^m(\cos \theta) - (n+1)(\alpha_1 \cos \theta + \alpha_2) \tilde{\mathcal{P}}_n^m(\cos \theta)]. \quad (57)$$

Finally, the l^{th} non-zero column $\frac{\partial \mathcal{B}(r_l) \mathbf{t}^H(\Psi_l)}{\partial \phi_l}$ involves the derivative of the scaled exponential function $\tilde{e}^{im\phi}$ which results in

$$\frac{\partial T_n^m(\Psi_l)}{\partial \phi_l} = im \beta T_n^m(\Psi_l). \quad (58)$$

The expressions in (55), (57) and (58) can be used to obtain $\bar{\mathbf{V}}_{\text{nm},r}$, $\bar{\mathbf{V}}_{\text{nm},\theta}$ and $\bar{\mathbf{V}}_{\text{nm},\phi}$ to calculate the CRB for near-field sources in the S^2H domain.

REFERENCES

- [1] W. Liu, M. Haardt, M. S. Greco, C. F. Mecklenbräuker, and P. Willett, "Twenty-five years of sensor array and multichannel signal processing: A review of progress to date and potential research directions," *IEEE Signal Processing Magazine*, vol. 40, no. 4, pp. 80–91, 2023.
- [2] R. Schmidt, "Multiple emitter location and signal parameter estimation," *IEEE transactions on antennas and propagation*, vol. 34, no. 3, pp. 276–280, 1986.
- [3] R. Roy and T. Kailath, "ESPRIT-estimation of signal parameters via rotational invariance techniques," *IEEE Transactions on acoustics, speech, and signal processing*, vol. 37, no. 7, pp. 984–995, 1989.
- [4] H. L. Van Trees, *Optimum array processing: Part IV of detection, estimation, and modulation theory*. John Wiley & Sons, 2002.
- [5] B. Rafaely, *Fundamentals of spherical array processing*. Springer, 2015, vol. 8.
- [6] —, "Plane-wave decomposition of the sound field on a sphere by spherical convolution," *The Journal of the Acoustical Society of America*, vol. 116, no. 4, pp. 2149–2157, 2004.
- [7] D. Khaykin and B. Rafaely, "Acoustic analysis by spherical microphone array processing of room impulse responses," *The Journal of the Acoustical Society of America*, vol. 132, no. 1, pp. 261–270, 2012.
- [8] D. Salvati, C. Drioli, and G. L. Foresti, "Diagonal unloading beamforming in the spherical harmonic domain for acoustic source localization in reverberant environments," *IEEE/ACM Transactions on Audio, Speech, and Language Processing*, vol. 28, pp. 2001–2012, 2020.
- [9] S. K. Yadav and N. V. George, "Sparse distortionless modal beamforming for spherical microphone arrays," *IEEE Signal Processing Letters*, vol. 29, pp. 2068–2072, 2022.
- [10] P. Lecomte, M. Melon, and L. Simon, "Spherical fraction beamforming," *IEEE/ACM Transactions on Audio, Speech, and Language Processing*, vol. 28, pp. 2996–3009, 2020.
- [11] S. K. Yadav and N. V. George, "Coarray manifold separation in the spherical harmonics domain for enhanced source localization," in *IEEE International Conference on Acoustics, Speech and Signal Processing (ICASSP)*, 2022, pp. 5038–5042.
- [12] S. Hafezi, A. H. Moore, and P. A. Naylor, "Augmented intensity vectors for direction of arrival estimation in the spherical harmonic domain," *IEEE/ACM Transactions on Audio, Speech, and Language Processing*, vol. 25, no. 10, pp. 1956–1968, 2017.

- [13] S. K. Yadav and N. V. George, "Speech enhancement via maximum likelihood modal beamforming with complex gaussian and laplacian priors," in *31st European Signal Processing Conference (EUSIPCO)*. IEEE, 2023, pp. 26–30.
- [14] X. Li, S. Yan, X. Ma, and C. Hou, "Spherical harmonics MUSIC versus conventional MUSIC," *Applied Acoustics*, vol. 72, no. 9, pp. 646–652, 2011.
- [15] H. Sun, H. Teutsch, E. Mabande, and W. Kellermann, "Robust localization of multiple sources in reverberant environments using EB-ESPRIT with spherical microphone arrays," in *IEEE International Conference on Acoustics, Speech and Signal Processing (ICASSP)*, 2011, pp. 117–120.
- [16] R. Goossens and H. Rogier, "Closed-form 2D angle estimation with a spherical array via spherical phase mode excitation and ESPRIT," in *IEEE International Conference on Acoustics, Speech and Signal Processing (ICASSP)*, 2008, pp. 2321–2324.
- [17] V. Varanasi, H. Gupta, and R. M. Hegde, "A deep learning framework for robust DOA estimation using spherical harmonic decomposition," *IEEE/ACM Transactions on Audio, Speech, and Language Processing*, vol. 28, pp. 1248–1259, 2020.
- [18] G. Ping, E. Fernandez-Grande, P. Gerstoft, and Z. Chu, "Three-dimensional source localization using sparse bayesian learning on a spherical microphone array," *The Journal of the Acoustical Society of America*, vol. 147, no. 6, pp. 3895–3904, 2020.
- [19] C. R. Landschoot and N. Xiang, "Model-based bayesian direction of arrival analysis for sound sources using a spherical microphone array," *The Journal of the Acoustical Society of America*, vol. 146, no. 6, pp. 4936–4946, 2019.
- [20] J. Capon, "High-resolution frequency-wavenumber spectrum analysis," *Proceedings of the IEEE*, vol. 57, no. 8, pp. 1408–1418, 1969.
- [21] E. Fisher and B. Rafaely, "The nearfield spherical microphone array," in *IEEE International Conference on Acoustics, Speech and Signal Processing (ICASSP)*, 2008, pp. 5272–5275.
- [22] —, "Near-field spherical microphone array processing with radial filtering," *IEEE Transactions on Audio, Speech, and Language Processing*, vol. 19, no. 2, pp. 256–265, 2010.
- [23] —, "Dolph-chebyshev radial filter for the near-field spherical microphone array," in *IEEE Workshop on Applications of Signal Processing to Audio and Acoustics*, 2009, pp. 169–172.
- [24] L. Kumar and R. M. Hegde, "Near-field acoustic source localization and beamforming in spherical harmonics domain," *IEEE Transactions on Signal Processing*, vol. 64, no. 13, pp. 3351–3361, 2016.
- [25] V. Varanasi, A. Agarwal, and R. M. Hegde, "Near-field acoustic source localization using spherical harmonic features," *IEEE/ACM Transactions on Audio, Speech, and Language Processing*, vol. 27, no. 12, pp. 2054–2066, 2019.
- [26] F. Ma, T. D. Abhayapala, and P. N. Samarasinghe, "A time-domain nearfield beamformer with spherical harmonic decomposition," *The Journal of the Acoustical Society of America*, vol. 154, no. 3, pp. 1850–1861, 2023.
- [27] Z. Li and R. Ruraiswami, "Hemispherical microphone arrays for sound capture and beamforming," in *IEEE Workshop on Applications of Signal Processing to Audio and Acoustics*, 2005, pp. 106–109.
- [28] D. Kumari and L. Kumar, "Acoustic source localization in hemispherical harmonics domain," in *Proc. EuroNoise*, 2018, pp. 2575–2580.
- [29] D. Kumari, V. Kailkhura, and L. Kumar, "Hemispherical harmonics based acoustic source localization in mixed-field," in *IEEE International Symposium on Signal Processing and Information Technology (ISSPIT)*, 2019, pp. 1–5.
- [30] D. Kumari and L. Kumar, "S²H domain processing for acoustic source localization and beamforming using microphone array on spherical sector," *IEEE Transactions on Signal Processing*, vol. 69, pp. 1983–1994, 2021.
- [31] —, "Spherical sector harmonics representation of sound fields using a microphone array over spherical sector," *The Journal of the Acoustical Society of America*, vol. 149, no. 1, pp. 145–157, 2021.
- [32] —, "Optimal beamformer design in spherical sector harmonics domain," *Applied Acoustics*, vol. 200, p. 109070, 2022.
- [33] —, "Computation of spherical sector harmonics norm with application to blind source separation," *JASA Express Letters*, vol. 3, no. 10, 2023.
- [34] H. Bi, F. Ma, T. D. Abhayapala, and P. N. Samarasinghe, "Spherical sector harmonics based directional drone noise reduction," in *2022 International Workshop on Acoustic Signal Enhancement (IWAENC)*. IEEE, 2022, pp. 1–5.
- [35] H. Bi, T. D. Abhayapala, F. Ma, and P. N. Samarasinghe, "Spherical sector harmonics based soundfield radial extrapolation and robustness analysis," in *ICASSP 2023-2023 IEEE International Conference on Acoustics, Speech and Signal Processing (ICASSP)*. IEEE, 2023, pp. 1–5.
- [36] P. M. Morse and K. U. Ingard, *Theoretical acoustics*. Princeton university press, 1986.
- [37] P. M. Morse and H. Feshbach, "Methods of theoretical physics," *American Journal of Physics*, vol. 22, no. 6, pp. 410–413, 1954.
- [38] E. G. Williams, *Fourier acoustics: sound radiation and nearfield acoustical holography*. Academic Press, 1999.
- [39] B. Rafaely, "Analysis and design of spherical microphone arrays," *IEEE Transactions on speech and audio processing*, vol. 13, no. 1, pp. 135–143, 2004.
- [40] L. Kumar and R. M. Hegde, "Stochastic cramer-rao bound analysis for DOA estimation in spherical harmonics domain," *IEEE Signal Processing Letters*, vol. 22, no. 8, pp. 1030–1034, 2014.
- [41] R. H. Hardin and N. J. Sloane, "Mclaren's improved snub cube and other new spherical designs in three dimensions," *Discrete & Computational Geometry*, vol. 15, pp. 429–441, 1996.
- [42] E. B. Saff and A. B. Kuijlaars, "Distributing many points on a sphere," *The mathematical intelligencer*, vol. 19, pp. 5–11, 1997.
- [43] X. Zhao, "System information class for windows. [Access on: December 2023]. [Online]. Available: <https://www.mathworks.com/matlabcentral/fileexchange/26662-system-information-class-for-windows>
- [44] T. Nakatani, T. Yoshioka, K. Kinoshita, M. Miyoshi, and B.-H. Juang, "Speech dereverberation based on variance-normalized delayed linear prediction," *IEEE Transactions on Audio, Speech, and Language Processing*, vol. 18, no. 7, pp. 1717–1731, 2010.
- [45] M. Abramowitz, I. A. Stegun, and R. H. Romer, "Handbook of mathematical functions with formulas, graphs, and mathematical tables," 1988.